INORGANIC CHEMISTRY FRONTIERS

RESEARCH ARTICLE

View Article Online
View Journal | View Issue





Cite this: *Inorg. Chem. Front.*, 2024, **11**, 5473

# Fluoride-free synthesis of high-silica RHO zeolite for the highly selective synthesis of methylamine†

Yufei Wang,‡[a] Jinfeng Han,‡[a] Keyan Jin,[a] Shuang Liu,[a] Qiang Li,[a] Pan Hou,[a] Shiping Liu,[b] Qi Song,[c] Zhendong Wang,[c] Peng Tian *[b] and Wenfu Yan *[a]

Low-silica **RHO** zeolites have been recognized as efficient catalysts for synthesizing industrial intermediates monomethylamine (MMA) and dimethylamine (DMA) through the reaction of methanol (MeOH) with ammonia. However, they typically suffer from rapid deactivation. Herein, we report the synthesis of high-silica **RHO** zeolite with small crystal sizes (1–2 μm) *via* interzeolite conversion of SSZ-13, utilizing a reduced amount of organic structure-directing agent (OSDA) and without the use of fluoride. It was demonstrated that the double eight-membered rings of **RHO** zeolite can be formed using the single eight-membered ring of SSZ-13, resulting in a reduction of OSDA dosage by approximately 30% and $Cs^+$ by about 38%. The resulting high-silica **RHO** zeolites exhibit an excellent methanol conversion of ~93%, a high MMA and DMA yield of ~90%, and good reaction durability under conditions more severe than those of industrial manufacture conditions, at 350 °C with a liquid hourly space velocity at 11.7 $h^{-1}$. Compared to directly synthesized high-silica **RHO** zeolites with larger crystal sizes (3–8 μm), interzeolite-converted high-silica **RHO** zeolites with smaller crystal sizes show a 10–16% higher yield of MMA and DMA. These findings highlight the significant potential of high-silica **RHO** zeolites for the industrial manufacturing of MMA and DMA.

Received 12th June 2024,
Accepted 20th July 2024

DOI: 10.1039/d4qi01467g

rsc.li/frontiers-inorganic

## 1. Introduction

Zeolites are microporous aluminosilicate crystals known for their uniform channels and adjustable Brønsted acid sites, making them valuable as adsorbents, ion-exchangers, and catalysts.[1–7] Among their applications, the selective synthesis of methylamine is a key zeolitic-catalyzed reaction for producing the widely used industrial intermediates monomethylamine (MMA) and dimethylamine (DMA) with high yields.[8] Traditionally, the industrial synthesis of methylamines involves the vapor-phase reaction of methanol (MeOH) with ammonia ($NH_3$) over amorphous silica-alumina catalysts (Brønsted acid catalysts) under harsh conditions. These conditions include high temperatures (around 400 °C), high pressures exceeding 2.0 MPa, and $NH_3$/MeOH mole ratios (N/C) ranging from 1 to 4.[9] However, this method tends to produce a higher proportion of the thermodynamically stable product, trimethylamine (TMA), rather than MMA or DMA.[10]

In the 1980s, **MOR** zeolite, featuring 12-ring (6.5 × 7.0 Å) and 8-ring (3.4 × 4.8 Å) channels, found application in the industrial production of methylamines.[11] However, the process required intricate post-treatments to decrease the 12-ring pore size, preventing the escape of TMA (3.9 × 5.4 × 6.1 Å) and thereby enhancing the selectivity of MMA (3.7 × 3.9 × 4.4 Å) and DMA (3.9 × 4.7 × 6.0 Å). These processing methods involved ion-exchange, steaming, and $SiCl_4$ treatment.[12,13] In pursuit of zeolites with pore sizes (3.0–4.5 Å) suitable for inhibiting TMA escape, attention has shifted to small-pore zeolites like **AFX**, **CHA**, **DDR**, **ERI**, **KFI**, **LEV**, **LTA**, **MTF**, **PWN**, **RHO**, and **UFI**.[14–17] Among these, **RHO** zeolite stands out due to its three-dimensional 8-ring channels and pore size of 3.6 × 3.6 Å, making it highly promising as a catalyst because of its exceptional MeOH conversion and high selectivity for MMA and DMA.[18,19]

In 1973, **RHO** zeolite with a Si/Al ratio of 2.9 was synthesized for the first time using CsOH as the inorganic structure-directing agent.[20] Subsequently, **RHO** zeolite with a higher Si/Al ratio of 3.9 was successfully synthesized using 18-crown-6 as the organic structure-directing agent (OSDA).[21] However, **RHO** zeolite (Si/Al = 3.4–4.1) experiences a significant

[a]*State Key Laboratory of Inorganic Synthesis and Preparative Chemistry, College of Chemistry, Jilin University, 2699 Qianjin Street, Changchun 130012, China. E-mail: yanw@jlu.edu.cn*
[b]*National Engineering Research Center of Lower-Carbon Catalysis, Dalian National Laboratory for Clean Energy, Dalian Institute of Chemical Physics, Chinese Academy of Sciences, Dalian 116023, China. E-mail: tianpeng@dicp.ac.cn*
[c]*State Key Laboratory of Green Chemical Engineering and Industrial Catalysis, Sinopec Shanghai Research Institute of Petrochemical Technology Co., Ltd, Shanghai 201208, China*

†Electronic supplementary information (ESI) available. See DOI: https://doi.org/10.1039/d4qi01467g

‡These authors contributed equally to this work.

drop in MMA and DMA yield (about 40%) and MeOH conversion (about 50%) after 10 h under harsh conditions of 400 °C, N/C = 1.0, and $WHSV_{MeOH}$ = 4.3 $h^{-1}$.[17] Investigations have revealed the formation of coke deposits on the zeolitic catalysts, although their detailed structures have not been identified.[17]

Previous studies have shown that increasing the Si/Al ratio of zeolitic catalyst reduces the number of Brønsted acid sites, which significantly mitigates deactivation but also slightly decreases MeOH conversion.[22] In the synthesis of high-silica **RHO** zeolite, methods involving dealumination and one-step synthesis are commonly employed.[17,23] Dealumination typically requires high-temperature steam treatment at 600–800 °C, which consumes substantial energy and raises safety concerns. In contrast, one-step synthesis has emerged as a promising method for high-silica **RHO** zeolite due to its milder synthesis conditions.[24–26] However, this approach, especially for high-silica **RHO** zeolite (Si/Al ≥ 4.9), often requires a significant quantity of OSDA, increasing catalyst cost and environmental pollution.[23,27] Additionally, when the Si/Al ratio of the **RHO** zeolite exceeds 8.0, the use of sodium fluoride is necessary, which poses environmental risks.[28] Hence, there is a pressing need to develop fluoride-free and less OSDA-intensive strategies for synthesizing high-silica **RHO** zeolite.

In addition to the Si/Al ratio, crystal size significantly impacts the catalytic performance of zeolitic catalysts.[29–31] Large crystal sizes have been reported to lead to decreased MeOH conversion.[32,33] Conventionally, high-silica **RHO** zeolites synthesized *via* one-step methods have crystal sizes ranging from 3–8 μm. Hence, there is a need to explore environmentally friendly methods to reduce crystal size.

In this study, high-silica **RHO** zeolites were synthesized *via* a one-pot interzeolite conversion of calcined SSZ-13 (**CHA**) zeolite under fluoride-free conditions and with reduced OSDA usage. The resulting high-silica **RHO** zeolites exhibited crystal sizes in the range of 1.2–1.4 μm and demonstrated excellent performance in the selective synthesis of methylamine, achieving MeOH conversion rates of 90–94% and MMA plus DMA yields of 87–91% under the condition of 350 °C, 2 MPa, N/C = 1.9 and $LHSV_{(MeOH+ammonia)}$ = 11.7 $h^{-1}$ ($GHSV_{(MeOH+ammonia)}$ = 7488 $h^{-1}$). These conditions are more severe than those typically used in industrial manufacturing ($LHSV_{(MeOH+ammonia)}$ = 2.0–3.0 $h^{-1}$). Compared to conventionally synthesized high-silica **RHO** zeolites, the environmentally friendly synthesis method yielded superior catalytic performance. This work presents a novel approach for synthesizing high-silica **RHO** zeolites with enhanced performance in the selective synthesis of methylamine.

## 2. Results and discussion

### 2.1 Characterization of high-silica RHO zeolites

The experimental details along with chemical and materials are provided in the ESI.† The high-silica **RHO** zeolites with Si/Al ratios of 8.7 and 7.3 (Table 1), synthesized *via* interzeolite conversion, are denoted as **RHO**-8.7 and **RHO**-7.3, respectively. In contrast, the reference high-silica **RHO** zeolites with Si/Al ratios of 7.9 and 6.7 (Table 1), synthesized *via* conventional methods,[23] are denoted as **RHO**-7.9C and **RHO**-6.7C, respectively, in which C indicating conventional. Fig. 1a displays the simulated XRD pattern of **RHO** zeolite alongside the experimental patterns of **RHO**-8.7, **RHO**-7.9C, **RHO**-7.3, and **RHO**-6.7C. The good agreement among them confirms that each synthesized high-silica **RHO** zeolite consists of a single phase. The $N_2$ adsorption isotherms at 77 K and texture properties of high-silica H-**RHO** zeolites are presented in Fig. 1b and Table S1,† respectively. As shown in Table S1,† the specific surface area and pore volume of high-silica H-**RHO** zeolites resulting from interzeolite conversion are comparable to those of directly synthesized high-silica **RHO** zeolites. Fig. 1c illustrates the $^{29}Si$ MAS NMR spectra of calcined **RHO** zeolites with various Si/Al ratios and seeds. The apparent signals centered at −109 ppm, −104 ppm, and −97 ppm are attributed to Si(0Al), Si(1Al), and Si(2Al), respectively.[34] With increasing Si/Al ratio of **RHO** zeolites, the signals assigned to Si(0Al) increase correspondingly, while the signal assigned to Si(2Al) gradually decreases. Fig. 1d presents the $^{27}Al$ MAS NMR spectra of calcined **RHO** zeolites with various Si/Al ratios. In all spectra, there is a single sharp signal centered at 59 ppm, corresponding to the characteristic peak of tetrahedral framework Al.[15] The absence of any signal around 0 ppm indicates the absence of octahedral extra-framework Al species in all high-silica **RHO** zeolites.[35]

Fig. 2 displays the SEM images of **RHO**-8.7, **RHO**-7.3, **RHO**-7.9C, and **RHO**-6.7C, with statistically analyzed average crystal sizes of 1.2 μm, 3.7 μm, 1.4 μm, and 7.8 μm, respectively. It is evident that the crystal sizes of the high-silica **RHO** zeolites synthesized *via* interzeolite conversion are smaller compared to those of high-silica **RHO** zeolites with similar Si/Al ratios synthesized directly.

The results of elemental analyses on high-silica **RHO** zeolites are summarized in Table 1. Previous studies have shown that **RHO** zeolite synthesis can involve alkali metal cations (*e.g.*, $Cs^+$), alkali metal cations combined with crown ether (*e.g.*, 18-crown-6), or alkali metal-crown ether complexes.[36,37] Due to their lower charge density, alkali metal-crown ether complexes (*e.g.*, $Cs^+$-18-crown-6) favor the formation of high-silica **RHO** zeolites.[23,28] In this study, an alkali metal cation-crown ether complex with the composition $(NaOH)_{1.4}\cdot(CsOH)\cdot(18\text{-crown-}6)_{2.2}\cdot(H_2O)_{10.2}$ is employed as the OSDA for synthesizing high-silica **RHO** zeolite. The compositions of the high-silica **RHO** zeolites, namely **RHO**-8.7 and **RHO**-7.3, as well as the reference high-silica **RHO** zeolites, **RHO**-7.9C and **RHO**-6.7C, are determined by combining elemental analyses and thermogravimetric (TG) analyses (Fig. S1†), detailed in Run 2, Run 5, Run 24, and Run 27 of Table 1, respectively. These analyses reveal that, on average, there are approximately one and a half 18-crown-6 molecules within the unit cell of high-silica **RHO** zeolites. Considering there are two *lta* cages in each unit cell, roughly 25% of *lta* cages remain unoccupied by 18-crown-6 molecules.

 

**Table 1** Synthesis conditions and elemental compositions of synthesized **RHO** samples (note: the name of each sample contains key information about the product and/or the variables of the synthetic parameters, including the Si/Al ratio of the zeolite, OSDA/$Al_2O_3$ ratio, seed loading, temperature, heating time, and whether fluoride was used, allowing for easy identification)

| Run | Sample | OSDA/$Al_2O_3$ | SSZ-13 | NaF | **RHO** seeds (wt% $SiO_2$) | Temperature/°C | Time/d | Crystalline phase | $C^a$ (wt%) | Si/Al$^b$ | Si/Al$^c$ | Na/Cs$^b$ |
|---|---|---|---|---|---|---|---|---|---|---|---|---|
| 1 | **RHO** seed[d] | 0.5 | – | – | 0 | 110 | 4 | **RHO** | 3.5 | 4.2 | 5.0 | 2.4 |
| **2** | **RHO-8.7**[e] | **2.8** | **+** | **–** | **12** | **150** | **4** | **RHO** | **6.2** | **8.7** | **8.5** | **1.2** |
| 3 | **RHO**-8.7-no seed[f] | 2.8 | + | – | 0 | 150 | 4 | **CHA** + Amor. | | | | |
| 4 | **RHO**-8.7-eq[g] | 2.8 | – | – | 12 | 150 | 4 | **LTL** + Amor. | | | | |
| **5** | **RHO-7.3**[h] | **2.2** | **+** | **–** | **10** | **150** | **4** | **RHO** | **6.1** | **7.3** | **6.9** | **1.2** |
| 6 | **RHO**-7.3-no seed[f] | 2.2 | + | – | 0 | 150 | 4 | **CHA** + Amor. | | | | |
| 7 | **RHO**-7.3-eq[g] | 2.2 | – | – | 10 | 150 | 4 | **LTL** + Amor. | | | | |
| 8 | **RHO**-8.7-15 | 2.8 | + | – | 15 | 150 | 4 | **RHO** | | 7.9 | | |
| 9 | **RHO**-8.7-3.0 | 3.0 | + | – | 12 | 150 | 4 | **RHO** | | 7.7 | | |
| 10 | **RHO**-8.7-3.5 | 3.5 | + | – | 12 | 150 | 4 | **RHO** | | 6.6 | | |
| 11 | **RHO**-7.3-15 | 2.2 | + | – | 15 | 150 | 4 | **RHO** | | 6.7 | | |
| 12 | **RHO**-7.3-2.5 | 2.5 | + | – | 10 | 150 | 4 | **RHO** | | 6.9 | | |
| 13 | **RHO**-7.3-3.0 | 3.0 | + | – | 10 | 150 | 4 | **RHO** | | 6.7 | | |
| 14 | **RHO**-8.7-180 | 2.8 | + | – | 12 | 180 | 4 | **RHO** + **ANA** | | | | |
| 15 | **RHO**-8.7-170 | 2.8 | + | – | 12 | 170 | 4 | **RHO** | | 8.4 | | |
| 16 | **RHO**-8.7-160 | 2.8 | + | – | 12 | 160 | 4 | **RHO** | | 8.7 | | |
| 17 | **RHO**-8.7-140 | 2.8 | + | – | 12 | 140 | 4 | **RHO** + **CHA** | | | | |
| 18 | **RHO**-8.7-140-8 | 2.8 | + | – | 12 | 140 | 8 | **RHO** + **CHA** | | | | |
| 19 | **RHO**-7.3-180 | 2.2 | + | – | 10 | 180 | 4 | **RHO** + **ANA** | | | | |
| 20 | **RHO**-7.3-170 | 2.2 | + | – | 10 | 170 | 4 | **RHO** | | 7.3 | | |
| 21 | **RHO**-7.3-160 | 2.2 | + | – | 10 | 160 | 4 | **RHO** | | 7.3 | | |
| 22 | **RHO**-7.3-140 | 2.2 | + | – | 10 | 140 | 4 | **RHO** + **CHA** | | | | |
| 23 | **RHO**-7.3-140-8 | 2.2 | + | – | 10 | 140 | 8 | **RHO** + **CHA** | | | | |
| **24** | **RHO-7.9C**[i] | **4.0** | **–** | **+** | **3** | **140** | **6** | **RHO** | **6.0** | **7.9** | **8.3** | **0.5** |
| 25 | **RHO**-7.9C-2.8-12[j] | 2.8 | – | + | 12 | 140 | 6 | **RHO** + Amor. | | | | |
| 26 | **RHO**-7.9C-2.8-12-no F[j] | 2.8 | – | – | 12 | 140 | 6 | **RHO** + Amor. | | | | |
| **27** | **RHO-6.7C**[k] | **3.3** | **–** | **–** | **3** | **140** | **6** | **RHO** | **6.0** | **6.7** | **6.7** | **0.7** |
| 28 | **RHO**-6.7C-2.2-10[j] | 2.2 | – | – | 10 | 140 | 6 | **RHO** + Amor. | | | | |

[a] Determined by the element analyses on the as-synthesized sample. [b] The contents of Na, Al and Si are determined by ICP analyses on the as-synthesized sample, the content of Cs is calculated according to the Na (ICP) and Al (ICP) content in the as-synthesized sample. [c] Determined by the $^{27}$Al MAS NMR and $^{29}$Si MAS NMR analyses on the calcined sample. [d] Un-calcined, and the unit cell composition is $Na_{6.6}Cs_{2.7}Al_{9.3}Si_{38.7}O_{96}\cdot$(18-crown-6)$_{1.0}\cdot 19.7H_2O$. [e] The unit cell composition is $Na_{2.7}Cs_{2.3}Al_{5.0}Si_{43}O_{96}\cdot$(18-crown-6)$_{1.6}\cdot 13.5H_2O$. [f] In the absence of **RHO** seeds. [g] Switch the parent zeolite SSZ-13 to the initial mixture containing the same components with the pseudo-boehmite as alumina source and the AS-40 as silica source. [h] The unit cell composition is $Na_{3.2}Cs_{2.6}Al_{5.8}Si_{42.2}O_{96}\cdot$(18-crown-6)$_{1.6}\cdot 12.2H_2O$. [i] The unit cell composition is $Na_{1.8}Cs_{3.7}Al_{5.5}Si_{42.5}O_{96}\cdot$(18-crown-6)$_{1.6}\cdot 8.9H_2O$. [j] Switch the parent zeolite SSZ-13 to the initial mixture containing the same components with the $NaAlO_2$ as alumina source and the AS-40 as silica source. [k] The unit cell composition is $Na_{2.7}Cs_{3.7}Al_{6.4}Si_{41.6}O_{96}\cdot$(18-crown-6)$_{1.6}\cdot 9.1H_2O$.

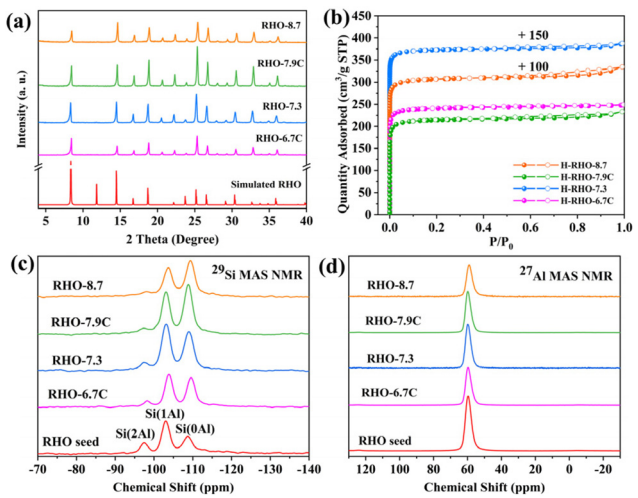


**Fig. 1** (a) Experimental and simulated XRD patterns of high-silica **RHO** zeolites, (b) $N_2$ adsorption isotherms of high-silica H-**RHO** samples; (c) $^{29}$Si MAS NMR spectra and (d) $^{27}$Al MAS NMR spectra of calcined **RHO** zeolites with different Si/Al ratios.

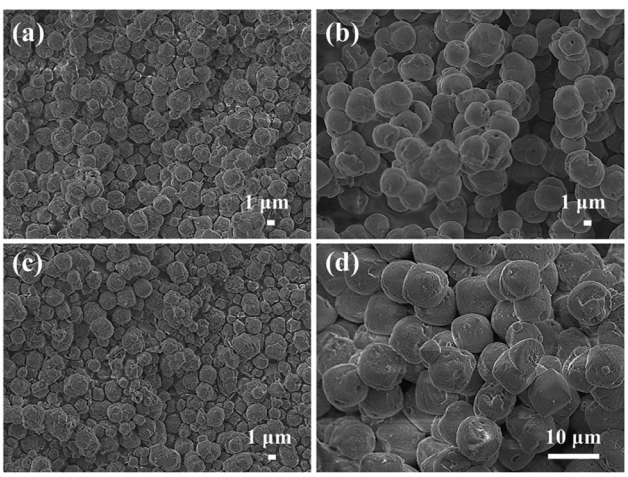


**Fig. 2** SEM images of (a) **RHO**-8.7, (b) **RHO**-7.9C, (c) **RHO**-7.3, and (d) **RHO**-6.7C.

### 2.2 Process of interzeolite conversion

The X-ray diffraction (XRD) patterns of the solid samples isolated throughout the crystallization of **RHO**-8.7 and **RHO**-7.3 are presented in Fig. 3a and b, respectively. In Fig. 3a, the intensity of the characteristic peaks of SSZ-13 ($2\theta$ = 9.7°, 13.1°, 14.2°, 18.0°, 23.4°, 26.3°, 28.5°, and 31.1°) gradually decreases, and an amorphous broad peak (15–30°, Fig. S2†) emerges within 2 d of heating, indicating the progressive decomposition of the long-range order of parent SSZ-13.[38,39] After heating for 3 d, the characteristic peaks of SSZ-13 are no longer visible, indicating complete dissolution. Due to the presence of **RHO** seeds, characteristic peaks of **RHO** zeolite at $2\theta$ = 8.4°, 18.8°, 26.7°, and 32.9° are observed in the XRD pattern of the isolated solid sample initially (0 h). As the crystallization progresses, the intensity of **RHO** zeolite peaks gradually increases, reaching a maximum at 4 d. Prolonging the crystallization time to 5 d does not increase the peak intensity, indicating the completion of **RHO**-8.7 crystallization after 4 d. Fig. 3b depicts the XRD patterns of solid samples isolated during **RHO**-7.3 crystallization, showing a similar behavior to **RHO**-8.7. Highly crystalline **RHO**-7.3 is obtained after 4 d of crystallization. Fig. 3c and d illustrate the evolution of relative crystallinity during the crystallization of **RHO**-8.7 and **RHO**-7.3, respectively. The relative crystallinity of the product is represented by the crystallization curve. These results align with the XRD patterns presented in Fig. 3a and b, respectively.

To investigate the evolution of structural building units during the interzeolite conversion of SSZ-13 zeolite to high-silica **RHO** zeolites, we analyzed solid samples isolated throughout the crystallization of **RHO**-8.7 and **RHO**-7.3 using FT-IR spectra, as shown in Fig. 4a and b, respectively. Previous investigations have assigned the IR bands at 676 $cm^{-1}$, 646 $cm^{-1}$ and 536 $cm^{-1}$, and 604 $cm^{-1}$ to the vibrations of s8r units,[40] d6r units,[41–43] and d8r units,[44] respectively. In Fig. 4a,

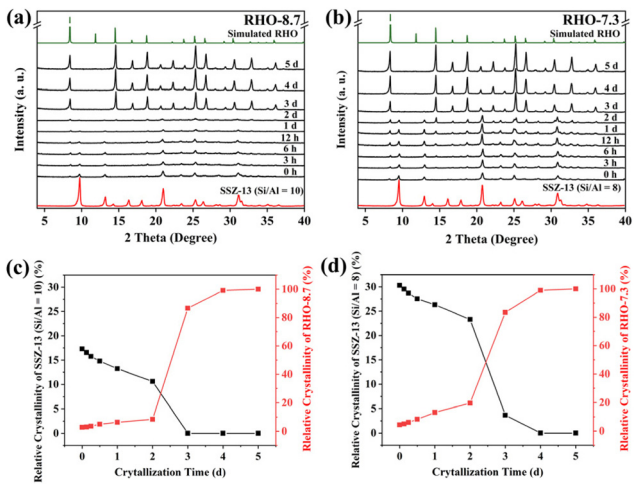


**Fig. 3** XRD patterns of the isolated solid samples throughout the crystallization of (a) **RHO**-8.7 and (b) **RHO**-7.3; SSZ-13/**RHO** zeolite relative crystallinity as a function of crystallization time during the interzeolite conversion of (c) **RHO**-8.7 and (d) **RHO**-7.3.

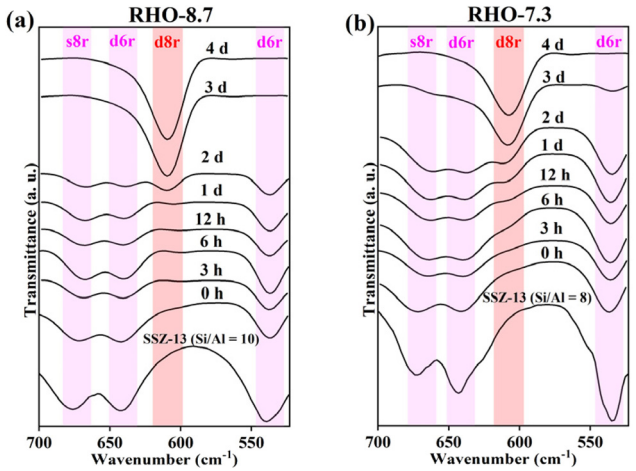


**Fig. 4** FT-IR spectra of the isolated solid samples throughout the crystallization of (a) **RHO**-8.7 and (b) **RHO**-7.3.

the IR bands corresponding to d6r units (646 $cm^{-1}$ and 536 $cm^{-1}$) and s8r units (676 $cm^{-1}$) completely disappear after 3 d of heating, indicating the complete decomposition of the parent SSZ-13 after 3 d of crystallization, consistent with the results in Fig. 3a. Meanwhile, the IR band associated with d8r units (604 $cm^{-1}$) is slightly detectable after 2 d of heating and becomes significant after 3 d of heating, indicating the formation and growth of **RHO**-8.7, which corroborates the results in Fig. 3a.

Fig. 4b illustrates the FT-IR spectra of solid samples isolated throughout the crystallization of **RHO**-7.3, showing similar variations in s8r units (676 $cm^{-1}$), d6r units (646 $cm^{-1}$ and 536 $cm^{-1}$), and d8r units (604 $cm^{-1}$). However, it is noteworthy that during the crystallization process of **RHO**-7.3, the IR bands corresponding to d6r units (646 $cm^{-1}$ and 536 $cm^{-1}$) and s8r units (676 $cm^{-1}$) completely vanish after 4 d of heating, compared to 3 d for **RHO**-8.7. This suggests that the parent SSZ-13 zeolite with a Si/Al ratio of 10 for **RHO**-8.7 decomposes faster than the parent SSZ-13 zeolite with a Si/Al ratio of 8 for **RHO**-7.3, likely due to the higher Si/Al zeolite being more easily dissolved under alkaline conditions.[45,46]

As depicted in Fig. 4a and b, the intensity of the band corresponding to s8r units (676 $cm^{-1}$) in SSZ-13 gradually diminishes, while the intensity of the band attributed to d8r units (604 $cm^{-1}$) in **RHO** zeolite rapidly increases during the crystallization process. It has been reported that the structural units of the parent zeolite can be retained and then transfer to the structural units of the daughter zeolite during the interzeolite conversion process.[47–49] A recent example is that the intrinsic s6r units in diatomite combine to form d6r units in SSZ-13 during the synthesis of SSZ-13 using diatomite as the source, significantly decreasing the crystallization time of SSZ-13.[50] According to the evolution of the FT-IR signals of s8r units and d8r units in Fig. 4, it can be inferred that the d8r units of **RHO** zeolite may originate from the fusion of the s8r units of the decomposed parent SSZ-13.

 

To further verify this hypothesis, UZM-12 (**ERI**) zeolite and SSZ-39 (**AEI**) zeolite, which possess similar frameworks to SSZ-13 and contain s8r units,[51–53] were used as parent zeolites for the synthesis of **RHO** zeolite through interzeolite conversion. When UZM-12 is used as the parent zeolite, after crystallization at 150 °C for 4 d, highly crystalline **RHO** zeolite is obtained (Fig. S3a†), even though the possible impurity of **ANA** zeolite also forms,[20,21] which strongly supports the hypothesis that s8r units in the parent zeolite combine to form d8r units of **RHO** zeolite. For SSZ-39 as the parent zeolite, despite the characteristic peaks of SSZ-39 appearing in the product, the presence of the characteristic peaks of **RHO** zeolite in the product also supports this speculation (Fig. S3b†). Additionally, the appearance of **MOR** zeolite by prolonging the heating time to 8 d (Fig. S3b†) suggests that **MOR** zeolite can also be synthesized during the crystallization of high-silica **RHO** zeolites.[54] Thus, it is inferred that parent zeolites containing s8r units are prone to converting into d8r units of **RHO** zeolite under suitable synthetic conditions, which also accounts for shortening the crystallization time in the interzeolite conversion process.

### 2.3 Factors affecting the crystallization of high-silica RHO zeolites

The detailed investigation of the influence of synthetic parameters on the interzeolite conversion crystallization of high-silica **RHO** zeolites is summarized in Table 1. First, the parent SSZ-13 (Si/Al = 10) was replaced by SSZ-13 with a higher Si/Al ratio of 35 to verify the universality of the interzeolite conversion of SSZ-13 to **RHO** zeolites. The appearance of the characteristic peaks of **RHO** zeolite in the XRD pattern of the product suggests that the interzeolite conversion from SSZ-13 to **RHO** zeolite is a universal process (Fig. S4a†). Subsequently, the role of the seed is examined (Run 2–7 in Table 1). Under optimal conditions, highly crystalline **RHO**-8.7 (Run 2) and **RHO**-7.3 (Run 5) are successfully synthesized. In the absence of **RHO** seed (Run 3 for **RHO**-8.7 and Run 6 for **RHO**-7.3), no **RHO** zeolite is formed, and the products contain the parent SSZ-13 zeolite along with an amorphous phase (Fig. S4b and S4c†). When the parent SSZ-13 zeolite is replaced with an initial mixture containing the same components but with pseudo-boehmite as the alumina source and AS-40 as the silica source (Run 4 for **RHO**-8.7 and Run 7 for **RHO**-7.3), the product contains **LTL** zeolite impurities along with an amorphous phase (Fig. S4†). This outcome underscores the essential role of the interzeolite conversion process in facilitating the formation of **RHO** zeolite.

In the interzeolite conversion process, the primary synthetic variables include the quantity of seeds and OSDA/$Al_2O_3$ ratio. Consequently, we explored the phase diagram, or crystallization field, of **RHO**-8.7 and **RHO**-7.3 by varying the OSDA/$Al_2O_3$ ratio and the amount of **RHO** seed. The results are illustrated in Fig. S5† (Fig. S5a† for **RHO**-8.7 and Fig. S5b† for **RHO**-7.3), with relevant details provided in Table 1. As observed in Fig. S5,† the formation of pure phases of **RHO**-8.7 and **RHO**-7.3 is determined by both the quantity of seeds and the OSDA/$Al_2O_3$ ratios. For **RHO**-8.7, the quantity of **RHO** seed is constrained to the range of 12–15% (Fig. S5a†). Additionally, the Si/Al ratio of these resulting pure **RHO** zeolites varies with changes in the OSDA/$Al_2O_3$ ratio and seed quantity (Run 8–10). Furthermore, the Si/Al ratio of these **RHO** zeolites is also influenced by the heating temperature and crystallization time (Run 15 and 16). To minimize the OSDA usage while attaining a high-silica **RHO** product, the optimal OSDA/$Al_2O_3$ ratio and amount of **RHO** seeds for **RHO**-8.7 are determined to be 2.8 and 12 wt% of $SiO_2$, respectively. For **RHO**-7.3, the quantity of **RHO** seed is constrained to the range of 10–15% (Fig. S5b†). Again, the Si/Al ratio of these resulting pure **RHO** zeolites varies (Run 11–13) and is influenced by the heating temperature and crystallization time (Run 20 and Run 21). The most suitable OSDA/$Al_2O_3$ ratio and amount of **RHO** seeds for **RHO**-7 are 2.2 and 10 wt% of $SiO_2$, respectively. Deviation from the optimal composition of the initial mixture can result in the preservation of the parent SSZ-13 zeolite and the formation of **MOR** zeolite (Table 1 and Fig. S5†).

Upon investigating the influence of heating temperature, 150 °C is identified as the optimal crystallization temperature (Table 1). The results presented in Table 1 and Fig. S5† demonstrate that a single phase of **RHO** zeolite with a Si/Al ratio of 8.7 can be achieved in Run 2 (150 °C) and Run 16 (160 °C), while a Si/Al ratio of 7.3 can be synthesized in Run 5 (150 °C), Run 20 (170 °C), and Run 21 (160 °C) through the interzeolite conversion of SSZ-13. Consequently, Run 2 and Run 5 are identified as the optimal conditions for **RHO**-8.7 and **RHO**-7.3, respectively.

In contrast, the reference high-silica **RHO** zeolite with a Si/Al ratio of 7.9 (**RHO**-7.9C) is directly synthesized from the initial mixture with an OSDA/$Al_2O_3$ ratio of 4.0 and in the presence of fluoride (Run 24).[23] Its composition is $Na_{1.8}Cs_{3.7}Al_{5.5}Si_{42.5}O_{96}\cdot(18\text{-crown-6})_{1.6}\cdot 8.9H_2O$. Another reference high-silica **RHO** zeolite with a Si/Al ratio of 6.7 (**RHO**-6.7C) is directly crystallized in the absence of fluoride (Run 27), with a composition determined as $Na_{2.7}Cs_{3.7}Al_{6.4}Si_{41.6}O_{96}\cdot(18\text{-crown-6})_{1.6}\cdot 9.1H_2O$. In the interzeolite conversion crystallization of **RHO**-8.7 ($Na_{2.7}Cs_{2.3}Al_{5.0}Si_{43}O_{96}\cdot(18\text{-crown-6})_{1.6}\cdot 13.5H_2O$), the OSDA/$Al_2O_3$ ratio is 2.8. Comparatively, the OSDA/$Al_2O_3$ ratio of 2.8 in the crystallization of **RHO**-8.7 is reduced by 30% compared to the OSDA/$Al_2O_3$ ratio of 4.0 in the synthesis of **RHO**-7.9C. Thus, the cost of **RHO**-8.7 is approximately 79% of **RHO**-7.9C based on the market price of the chemicals. Furthermore, the amount of $Cs^+$ in the interzeolite-converted **RHO**-8.7 is 38% less than that in the directly synthesized reference **RHO**-7.9C zeolites. Similarly, in the synthesis of RHO-7.3, the OSDA/$Al_2O_3$ ratio of 2.2 is reduced by 33% compared to the OSDA/$Al_2O_3$ ratio of 3.3 in another reference high-silica **RHO**-6.7C. Thus, the cost of **RHO**-7.3 is approximately 81% of **RHO**-6.7C based on the market price of the chemicals, and the amount of $Cs^+$ in the interzeolite-converted **RHO**-7.3 is reduced by 30% compared with the directly synthesized reference **RHO**-6.7C zeolites. When the OSDA/$Al_2O_3$ ratio of 4.0 and the seed loading of 3% in Run 24 (the optimal recipe for **RHO**-7.9C

reported[23]) are decreased to 2.8 and increased to 12%, respectively, amorphous phase is obtained alongside crystalline **RHO** zeolite (Run 25 and Run 26). Similar results are observed for **RHO**-6.7C (Run 27 and Run 28). These findings suggest that the formation process of high-silica **RHO** zeolite in the interzeolite conversion synthesis differs from that in direct synthesis. Moreover, interzeolite conversion synthesis requires significantly less OSDA and $Cs^+$ than the direct synthesis approach due to the sufficient s8r species in the interzeolite conversion approach from the decomposition of the parent SSZ-13 zeolite. The s8r species can further form d8r building units *via* fusion, the basic building units of **RHO** zeolite, aligning with the results obtained from FT-IR spectra. In contrast, in the direct synthesis approach, the formation of d8r building units necessitates direction by $Cs^+$ and/or $Cs^+$-crown ether complex, leading to greater consumption of $Cs^+$ and crown ether.

### 2.4 Catalytic performance of high-silica RHO zeolites

The catalytic performance of H-**RHO**-8.7 and H-**RHO**-7.3 in the selective synthesis of methylamine was investigated, and the corresponding results are summarized in Table 2. The details of catalytic conditions are provided in the ESI.† For comparison, the catalytic performance of other zeolites reported in the literatures under typical catalytic conditions (350 °C, N/C = 2, normal pressure, $WHSV_{MeOH}$ = 0.813 $h^{-1}$, $GHSV_{(MeOH+ammonia)}$ = 698 $h^{-1}$; 400 °C, N/C = 1, normal pressure, $WHSV_{MeOH}$ = 4.3 $h^{-1}$, $GHSV_{(MeOH+ammonia)}$ = 3972 $h^{-1}$) is also included in Table 2. These zeolites include H-**MOR** zeolite, a commercial catalyst for the selective synthesis of methylamine,[55] H-ZK-5 (**KFI**),[15] H-PST-29 (**PWN**),[56] and SAPO-34 (**CHA**).[18] Table 2 indicates that the MMA plus DMA yield of the **RHO** zeolitic catalysts (H-**RHO**-8.7, H-**RHO**-7.3, and H-**RHO**) is higher than that of the other zeolitic catalysts, suggesting that **RHO** zeolite has advantages for the selective synthesis of methylamine *via* the vapor-phase reaction of MeOH with $NH_3$.[12,13,19]

Under the harsh catalytic conditions (400 °C, $WHSV_{MeOH}$ = 4.3 $h^{-1}$, and N/C molar ratio of 1 for the feed gas), the H-**RHO** with a Si/Al ratio of 4.1 exhibits the highest MMA plus DMA yield of approximately 84% after 1 h of reaction. However, this yield dramatically drops to around 45% after 10 h of reaction. In comparison, under the same harsh catalytic conditions, the MMA plus DMA yield of H-**RHO**-8.7 and H-**RHO**-7.3 changes by less than 1.0% after 10 h. The significant deactivation of the zeolitic catalysts after 10 h of reaction is also observed in low-silica zeolites, including H-PST-29 (Si/Al = 5.0) and H-**MOR** (Si/Al = 5.0). The MMA plus DMA yield of H-PST-29 and H-**MOR** decreases from approximately 52% and 32% to about 40% and 30%. This rapid deactivation can be attributed to the low-silica nature of these zeolites, which may result in a higher density of Brønsted acid sites and consequently a faster formation of organic deposits compared to the high-silica H-**RHO** zeolites.[57–59]

It is well recognized that the dealumination of low-silica zeolites can improve the framework Si/Al ratio and mitigate the catalyst deactivation.[17] However, compared to the corresponding low-silica zeolites, the resultant high-silica zeolites often exhibit lower crystallinity and reduced activity (Table 2).[60] For instance, when the Si/Al ratio of H-**RHO** and H-PST-29 is increased to 11.0 and 12.0 from 4.1 and 5.0 through dealumination, respectively, the MMA plus DMA yield of the dealuminated samples after 10 h of reaction under the same harsh conditions (400 °C, $WHSV_{MeOH}$ = 4.3 $h^{-1}$, N/C = 1) decreases to approximately 55% and 53% from around 71% and 61%, respectively. In contrast, the high-silica H-**RHO** zeolites synthesized *via* interzeolite conversion exhibit significantly greater durability than all other zeolitic catalysts, indicating that H-**RHO**-8.7 and H-**RHO**-7.3 hold great potential for industrial applications.

To determine the optimal reaction temperature for the selective synthesis of methylamine, we investigated the catalytic performance of H-**RHO**-8.7 and H-**RHO**-7.3 in the temperature range of 250–400 °C. The results for MeOH conversion, yield of MMA plus DMA, selectivity of MMA plus DMA, and selectivity of TMA are presented in Fig. 5, respectively. Overall, the influence of reaction temperature on the catalytic performance of H-**RHO**-8.7 is similar to that on the catalytic performance of H-**RHO**-7.3. As illustrated in Fig. 5a, the MeOH conversion of H-**RHO**-8.7 and H-**RHO**-7.3 rapidly increases from 20–30% at 250 °C to 97–98% at 350 °C. Further increasing the reaction temperature to 400 °C results in a MeOH conversion of 99%. Considering that the 1% increase in MeOH conversion with a 50 °C temperature increase is not significant, 350 °C is recommended as the optimal reaction temperature for both H-**RHO**-8.7 and H-**RHO**-7.3. Moreover, the yield of MMA plus DMA for both H-**RHO**-8.7 and H-**RHO**-7.3 reaches its maximum at 350 °C (Fig. 5b). The selectivity for MMA plus DMA peaks at 350 °C for H-**RHO**-7.3, while for H-**RHO**-8.7, the maximum selectivity is observed at 300 °C (Fig. 5c). Similar to MeOH conversion, the selectivity for TMA increases with rising reaction temperature for both zeolites (Fig. 5d). These results suggest that 350 °C is an optimum reaction temperature for the selective synthesis of methylamine over H-**RHO**-8.7 and H-**RHO**-7.3.

To assess the potential of high-silica H-**RHO** zeolites for industrial applications, we investigated their catalytic performance under condition of 350 °C, 2 MPa, $LHSV_{(MeOH+ammonia)}$ = 11.7 $h^{-1}$ ($GHSV_{(MeOH+ammonia)}$ = 7488 $h^{-1}$), and N/C = 1.9, which are significantly more severe than industrial conditions ($LHSV_{(MeOH+ammonia)}$ = 2.0–3.0 $h^{-1}$ (ref. 61)). The evaluated zeolites included the interzeolite converted H-**RHO**-8.7 and H-**RHO**-7.3, as well as the directly synthesized H-**RHO**-7.9C and H-**RHO**-6.7C. Fig. 6 depicts the MeOH conversion (Fig. 6a), yield of MMA plus DMA (Fig. 6b), selectivity of MMA plus DMA (Fig. 6c), and selectivity of TMA (Fig. 6d) for these four high-silica H-**RHO** zeolites. All high-silica H-**RHO** zeolites exhibit high activity and selectivity for MMA plus DMA during the reaction. After 6 h on stream, the reduction in yield and selectivity is negligible, indicating excellent durability for all four high-silica H-**RHO** zeolites. According to Fig. 6a, the interzeolite-converted H-**RHO**-8.7 and H-**RHO**-7.3 exhibit approximately 10% higher activity than the directly synthesized reference H-**RHO**-7.9C and H-**RHO**-6.7C,

 

**Table 2** Comparison of catalytic performances of zeolitic catalysts on selective synthesis of methylamine under various conditions

| Sample | Si/Al | Time on Stream (h) | N/C[b] | Temperature (°C) | $WHSV_{MeOH}$ ($h^{-1}$) | MeOH Conversion (%) | Selectivity (%) MMA plus DMA[c] | Selectivity (%) TMA | MMA plus DMA Yield[d] (%) | Ref. |
|---|---|---|---|---|---|---|---|---|---|---|
| **H-RHO-8.7** | **9.3**[a] | **3.0** | **2** | **350** | **0.813** | **96.77** | **77.85** | **13.59** | **75.34** | **This Work** |
| **H-RHO-7.3** | **7.5**[a] | **3.0** | **2** | **350** | **0.813** | **98.05** | **75.54** | **12.99** | **74.07** | **This Work** |
| H-ZK-5 | 3.2 | 3.0 | 2 | 350 | 0.813 | 63.4 | 86.2 | 5.1 | 54.7 | 15 |
| H-ZK-5 (K, Cs) | 2.9 | 3.0 | 2 | 350 | 0.813 | 69.5 | 80.0 | 7.6 | 55.6 | 15 |
| SAPO-34 | 0.4 | 2.8 | 2 | 350 | 0.813 | 51.07 | 83.13 | 10.40 | 42.45 | 18 |
| **H-RHO-8.7** | **9.3**[a] | **1.0** | **1** | **400** | **4.3** | **97.35** | **68.09** | **18.22** | **66.29** | **This work** |
| **H-RHO-8.7** | **9.3**[a] | **10.0** | **1** | **400** | **4.3** | **95.87** | **68.18** | **11.05** | **65.36** | **This work** |
| **H-RHO-7.3** | **7.5**[a] | **1.0** | **1** | **400** | **4.3** | **98.04** | **70.00** | **18.86** | **68.63** | **This work** |
| **H-RHO-7.3** | **7.5**[a] | **10.0** | **1** | **400** | **4.3** | **96.93** | **71.63** | **13.31** | **69.43** | **This work** |
| H-**RHO** | 4.1 | 1.0 | 1 | 400 | 4.3 | ~97 | ~87 | ~13 | ~84 | 17 |
| H-**RHO** | 4.1 | 10.0 | 1 | 400 | 4.3 | ~50 | ~90 | ~10 | ~45 | 17 |
| H-PST-29 | 5.0 | 1.0 | 1 | 400 | 4.3 | ~65 | ~80 | ~20 | ~52 | 17 |
| H-PST-29 | 5.0 | 10.0 | 1 | 400 | 4.3 | ~48 | ~83 | ~17 | ~40 | 17 |
| H-**RHO** (dealuminated) | 11.0 | 1.0 | 1 | 400 | 4.3 | ~80 | ~88 | ~12 | ~71 | 17 |
| H-**RHO** (dealuminated) | 11.0 | 10.0 | 1 | 400 | 4.3 | ~62 | ~88 | ~12 | ~55 | 17 |
| H-PST-29 (dealuminated) | 12.0 | 1.0 | 1 | 400 | 4.3 | ~73 | ~84 | ~16 | ~61 | 17 |
| H-PST-29 (dealuminated) | 12.0 | 10.0 | 1 | 400 | 4.3 | ~65 | ~82 | ~18 | ~53 | 17 |
| H-**MOR** | 5.0 | 1.0 | 1 | 400 | 4.3 | ~70 | ~46 | ~54 | ~32 | 17 |
| H-**MOR** | 5.0 | 10.0 | 1 | 400 | 4.3 | ~60 | ~50 | ~50 | ~30 | 17 |

[a] Determined by the ICP analyses. [b] Molar ratio of the feed gas composition. [c] MMA plus DMA selectivity in all carbon base products. [d] MMA plus DMA yield = MeOH conversion × MMA plus DMA selectivity in all carbon base products.

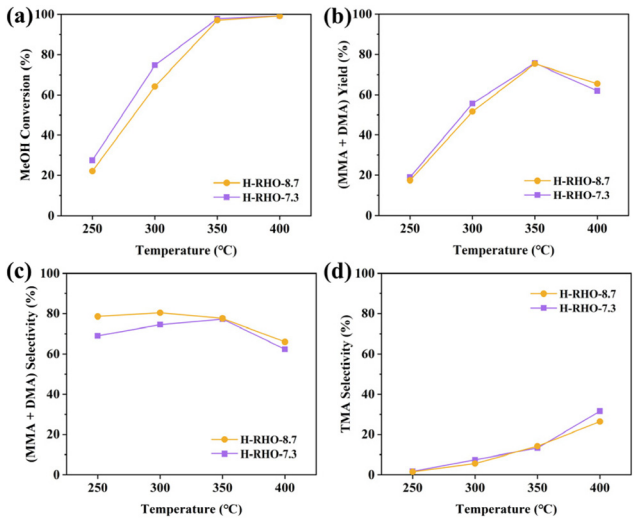


**Fig. 5** (a) MeOH conversion, (b) yield of MMA plus DMA, (c) selectivity of MMA plus DMA and (d) selectivity of TMA in the selective synthesis of methylamine catalyzed by H-**RHO**-8.7 and H-**RHO**-7.3 at reaction temperature of 250–400 °C, normal pressure, N/C = 2, $WHSV_{MeOH}$ = 0.813 $h^{-1}$ ($GHSV_{(MeOH+ammonia)}$ = 698 $h^{-1}$), and time on stream = 2.0 h.

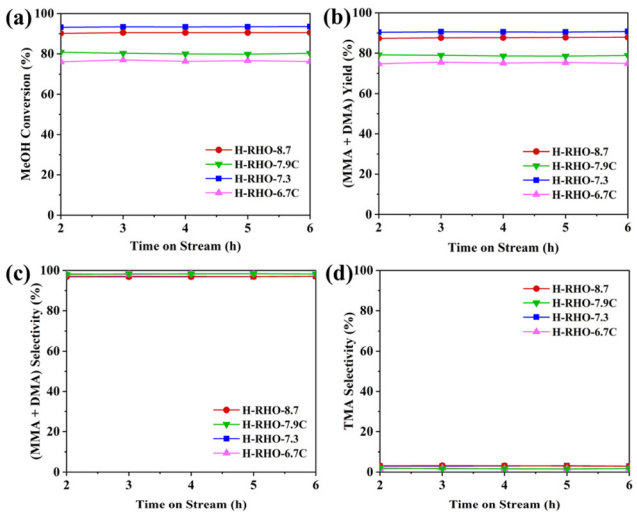


**Fig. 6** (a) MeOH conversion, (b) yield of MMA plus DMA, (c) selectivity of MMA plus DMA and (d) selectivity of TMA in selective synthesis of methylamine of high-silica H-**RHO** zeolites under the condition of severe manufacture at 350 °C, 2 MPa, N/C = 1.9 and $LHSV_{(MeOH+ammonia)}$ = 11.7 $h^{-1}$ ($GHSV_{(MeOH+ammonia)}$ = 7488 $h^{-1}$).

suggesting that high-silica **RHO** zeolites formed *via* interzeolite conversion possess unique features that enhance MeOH conversion. In contrast to the results in Fig. 5d, the TMA selectivity of the four high-silica H-**RHO** zeolites under condition of 350 °C, 2 MPa, N/C = 1.9, and $LHSV_{(methanol+ammonia)}$ = 11.7 $h^{-1}$ ($GHSV_{(MeOH+ammonia)}$ = 7488 $h^{-1}$) is only 2–3% (Fig. 6d). This indicates that higher space velocity can suppress TMA formation by promoting the release of MMA and DMA from active sites, thereby preventing further reactions between DMA and MeOH to form TMA.[62] Consequently, increasing the space velocity can

enhance selectivity for MMA plus DMA and reduce selectivity for TMA.[13]

As mentioned earlier, the formation of methylamines through the vapor-phase reaction of MeOH with $NH_3$ relies heavily on Brønsted acid sites, which significantly influence the catalytic activity. To gain further insights into the catalytic behavior of these high-silica H-**RHO** zeolites, $NH_3$-TPD analyses were conducted on H-**RHO**-8.7, H-**RHO**-7.9C, H-**RHO**-7.3, and H-**RHO**-6.7C. The $NH_3$-TPD profiles are provided in Fig. S6.† Upon deconvolution, three peaks emerged, centered at 160–180 °C, 210–230 °C, and 490–550 °C, corresponding to $NH_3$ desorption from weak, medium, and strong acid sites, respectively. The precise peak center and area of each profile are summarized in Table S2.† According to the literature, medium acid sites are the active sites for methylamine production during synthesis, whereas strong acid sites produce the side-product DME.[63] Notably, the resultant DME can further convert to methylamine during industrial conditions or more severe conditions, explaining why the four high-silica **RHO** zeolites exhibit almost identical selectivity for MMA plus DMA (Fig. 6c).[13] Thus, it can be concluded that both medium and strong acid sites are important factors on the catalytic performance of methylamine production. According to the acidic properties of the four high-silica H-**RHO** zeolites list in Table S2,† the order of the amounts of medium and strong acid sites is H-**RHO**-6.7C > H-**RHO**-7.3C > H-**RHO**-8.7 > H-**RHO**-7.9C. Interestingly, the order of MeOH conversion in Fig. 6a is H-**RHO**-7.3 > H-**RHO**-8.7 > H-**RHO**-7.9C > H-**RHO**-6.7C, which is inconsistent with the order of the amounts of medium and strong acid sites, suggesting the presence of other contributing factors affecting MeOH conversion.

Previous studies have demonstrated that mass transfer in microporous zeolites can significantly impact their applications in catalysis.[31] The interactions between zeolite channels and guest molecules increase transport resistance and affect the MeOH conversion.[30] Thus, decreasing the crystal sizes of zeolites would be beneficial for improving mass transfer, thereby enhancing MeOH conversion. In this study, the average crystal sizes of **RHO**-8.7, **RHO**-7.3, **RHO**-7.9C, and **RHO**-6.7C are 1.2, 1.4, 3.7, and 7.8 μm, respectively (Fig. 2). Among high-silica **RHO** zeolites with similar crystal sizes, H-**RHO**-7.3, with a larger amount of medium and strong acid sites (Table S2†), demonstrates higher MeOH conversion (~93%) than H-**RHO**-8.7 (~90%). This indicates that a higher amount of medium and strong acid sites results in higher MeOH conversion among zeolitic catalysts with similar crystal sizes. However, although H-**RHO**-6.7C has more medium and strong acid sites than the other catalysts (Table S2†), it shows a lower MeOH conversion (~76%) compared to H-**RHO**-7.9C (~80%). This is likely due to H-**RHO**-6.7C having a much larger crystal size (7.8 μm) than H-**RHO**-7.9C (3.7 μm). This indicates that larger crystal size leads to lower MeOH conversion when zeolitic catalysts have similar medium and strong acid sites. Thus, it can be concluded that both the amounts of medium and strong acid sites and the crystal size are the important factors affecting MeOH conversion. Considering the amounts of medium and strong acid sites in H-**RHO**-7.3 and H-**RHO**-8.7 are basically equal to or less than those of H-**RHO**-6.7C and H-**RHO**-7.9C, the crystal sizes of H-**RHO**-7.3 and H-**RHO**-8.7 are smaller than those of **RHO**-6.7C and **RHO**-7.9C, and the MeOH conversion of H-**RHO**-7.3 and H-**RHO**-8.7 is higher than that of H-**RHO**-6.7C and H-**RHO**-7.9C, it is clear that smaller crystal size leads to better mass transfer properties, which is likely the reason for the higher MeOH conversion of H-**RHO**-7.3 and H-**RHO**-8.7 compared to H-**RHO**-6.7C and H-**RHO**-7.9C.

## 3. Conclusions

In this study, we devised an environmentally friendly interzeolite conversion method to synthesize high-silica **RHO** zeolites with Si/Al ratios of 8.7 (**RHO**-8.7) and 7.3 (**RHO**-7.3). This method facilitates the transformation of SSZ-13 zeolite into high-silica **RHO** zeolites with crystal sizes ranging from 1 to 2 μm, achieved without the use of fluoride and with a reduced amount of OSDA by approximately 30% and $Cs^+$ by approximately 38% compared to the direct synthesis method. This reduction may be attributed to the formation of d8r through the fusion of s8r units resulting from the decomposition of SSZ-13. In contrast, the direct synthesis of high-silica **RHO** zeolites relies on the direction of these s8r units by a significant amount of OSDA. The interzeolite-converted high-silica **RHO** zeolites exhibit high activity in the selective synthesis of methylamine, owing to their appropriate amounts of acid sites and relatively small crystal sizes. Under the condition (350 °C, 2 MPa, N/C = 1.9, $LHSV_{(MeOH+ammonia)}$ = 11.7 $h^{-1}$, $GHSV_{(MeOH+ammonia)}$ = 7488 $h^{-1}$) which is more severe than industrial conditions ($LHSV_{(MeOH+ammonia)}$ = 2.0–3.0 $h^{-1}$), the MeOH conversion reaches approximately 93%, with a yield of approximately 90% and a selectivity of 97% for MMA plus DMA. Additionally, the selectivity for TMA is approximately 3%. No deactivation is observed after 6 h of reaction. The outstanding catalytic performance of the interzeolite-converted high-silica **RHO** zeolite positions it as a promising industrial catalyst for the selective synthesis of methylamines *via* the vapor-phase reaction of methanol with $NH_3$.

## Data availability

The data supporting this article have been included as part of the ESI.†

## Conflicts of interest

There are no conflicts to declare.

 

## Acknowledgements

We acknowledge the financial support from the National Key Research and Development Program of China (2021YFA1500401, 2021YFA1501202, 2022YFB3504000), the National Natural Science Foundation of China (22288101, 21991091), and the '111 Center' (B17020) for supporting this work.

## References

1 R. Xu, W. Pang, J. Yu, Q. Huo and J. Chen, *Chemistry of zeolites and related porous materials: Synthesis and structure*, John Wiley & Sons (Asia) Pte Ltd, Singapore, 2007.
2 W. Yan and J. Yu, Our journey in zeolite science, *Microporous Mesoporous Mater.*, 2023, **358**, 112368.
3 B. Wang, J. Li, X. Zhou, W. Hao, S. Zhang, C. Lan, X. Wang, Z. Wang, J. Xu, J.-N. Zhang, X. Li and W. Yan, Facile activation of lithium slag for the hydrothermal synthesis of zeolite A with commercial quality and high removal efficiency for the isotope of radioactive $^{90}Sr$, *Inorg. Chem. Front.*, 2022, **9**, 468–477.
4 J. Cejka, A. Corma and S. I. Zones, *Zeolites and catalysis: Synthesis, reactions and applications*, WILEY-VCH Verlag GmbH & Co. KGaA, Weinheim, 2010.
5 W. Hao, X. Yan, X. Guo, W. Wang, T. Yan, J.-N. Zhang and W. Yan, Synthesis of a low-silica **CHA** zeolite with exceptional selectivity for radioactive $^{137}Cs^{+}$, *Inorg. Chem. Front.*, 2023, **10**, 1894–1906.
6 S. Kulprathipanja, *Zeolites in industrial separation and catalysis*, WILEY-VCH Verlag GmbH & Co. KGaA, Weinheim, 2010.
7 Y. Wang, P. Bai, Z. Jin, Y. Li, Y. Li, W. Shi, X. Zhou, J. Xu, W. Yan and R. Xu, Stellerite-seeded facile synthesis of zeolite heulandite with exceptional aqueous $Cd^{2+}$ capture performance, *Inorg. Chem. Front.*, 2019, **6**, 1785–1792.
8 M. Dusselier and M. E. Davis, Small-pore zeolites: Synthesis and catalysis, *Chem. Rev.*, 2018, **118**, 5265–5329.
9 F. J. Weigert, Selective synthesis and equilibration of methylamines on sodium mordenite, *J. Catal.*, 1987, **103**, 20–29.
10 H. Matsuhashi and A. Futamura, Determination of relative acid strength and acid amount of solid acids by Ar adsorption, *Catal. Today*, 2006, **111**, 338–342.
11 Y. Ashina, T. Fujita, M. Fukatsu, K. Niwa and J. Yagi, Manufacture of dimethylamine using zeolite catalyst, *Stud. Surf. Sci. Catal.*, 1986, **28**, 779–786.
12 H.-Y. Jeon, C.-H. Shin, H. J. Jung and S. B. Hong, Catalytic evaluation of small-pore molecular sieves with different framework topologies for the synthesis of methylamines, *Appl. Catal., A*, 2006, **305**, 70–78.
13 D. R. Corbin, S. Schwarz and G. C. Sonnichsen, Methylamines synthesis: A review, *Catal. Today*, 1997, **37**, 71–102.
14 M. C. Ilao, H. Yamamoto and K. Segawa, Shape-selective methylamine synthesis over small-pore zeolite catalysts, *J. Catal.*, 1996, **161**, 20–30.
15 R. Wu, J. Han, Y. Wang, M. Chen, P. Tian, X. Zhou, J. Xu, J.-N. Zhang and W. Yan, Exclusive SAPO-seeded synthesis of ZK-5 zeolite for selective synthesis of methylamines, *Inorg. Chem. Front.*, 2022, **9**, 5766–5773.
16 R. D. Shannon, M. Keane, L. Abrams, R. H. Staley, T. E. Gier, D. R. Corbin and G. C. Sonnichsen, Selective synthesis of dimethylamine over small-pore zeolites I. H-Rho, *J. Catal.*, 1988, **113**, 367–382.
17 H. Lee, K. Lee, J. Shin and S. B. Hong, A comparative study of methylamines synthesis over zeolites H-rho and H-PST-29, *Microporous Mesoporous Mater.*, 2020, **300**, 110150.
18 Y. Qiao, P. Wu, X. Xiang, M. Yang, Q. Wang, P. Tian and Z. Liu, SAPO-34 synthesized with n-butylamine as a template and its catalytic application in the methanol amination reaction, *Chin. J. Catal.*, 2017, **38**, 574–582.
19 L. H. Callanan, C. T. O'Connor and E. van Steen, The effect of the adsorption properties of steamed zeolite rho on its methanol amination activity, *Microporous Mesoporous Mater.*, 2000, **35–36**, 163–172.
20 H. E. Robson, D. P. Shoemaker, R. A. Ogilvie and P. C. Manor, Synthesis and crystal structure of zeolite rho - a new zeolite related to Linde Type A, *Adv. Chem. Ser.*, 1973, **121**, 106–115.
21 T. Chatelain, J. Patarin, E. Fousson, M. Soulard, J. L. Guth and P. Schulz, Synthesis and characterization of high-silica zeolite **RHO** prepared in the presence of 18-crown-6 ether as organic template, *Microporous Mater.*, 1995, **4**, 231–238.
22 U. Olsbye, S. Svelle, K. P. Lillerud, Z. H. Wei, Y. Y. Chen, J. F. Li, J. G. Wang and W. B. Fan, The formation and degradation of active species during methanol conversion over protonated zeotype catalysts, *Chem. Soc. Rev.*, 2015, **44**, 7155–7176.
23 Q. Ke, T. Sun, X. Wei, Y. Guo, S. Xu and S. Wang, Economical synthesis strategy of **RHO** zeolites with fine-tuned composition and porosity for enhanced trace $CO_2$ capture, *Chem. Eng. J.*, 2019, **359**, 344–353.
24 G. A. Nasser, O. Muraza, T. Nishitoba, Z. Malaibari, T. K. Al-Shammari and T. Yokoi, OSDA-free chabazite (**CHA**) zeolite synthesized in the presence of fluoride for selective methanol-to-olefins, *Microporous Mesoporous Mater.*, 2019, **274**, 277–285.
25 J. H. Kang, F. H. Alshafei, S. I. Zones and M. E. Davis, Cage-defining ring: A molecular sieve structural indicator for light olefin product distribution from the methanol-to-olefins reaction, *ACS Catal.*, 2019, **9**, 6012–6019.
26 Y. Ji, J. Birmingham, M. A. Deimund, S. K. Brand and M. E. Davis, Steam-dealuminated, OSDA-free **RHO** and **KFI**-type zeolites as catalysts for the methanol-to-olefins reaction, *Microporous Mesoporous Mater.*, 2016, **232**, 126–137.
27 Q. Ke, T. Sun, H. Cheng, X. Wei, Y. Guo, S. Zhao, S. Zeng and S. Wang, Accelerated construction of high-silica **RHO** and **CHA** zeolites via interzeolite transformation and their

$NH_3$-SCR performances after copper exchange, *Ind. Eng. Chem. Res.*, 2018, **57**, 16763–16771.
28 Q. Ke, T. Sun, H. Cheng, H. Chen, X. Liu, X. Wei and S. Wang, Targeted synthesis of ultrastable high-silica **RHO** zeolite through alkali metal-crown ether interaction, *Chem. – Asian J.*, 2017, **12**, 1043–1047.
29 A. Palčić and E. Catizzone, Application of nanosized zeolites in methanol conversion processes: A short review, *Curr. Opin. Green Sustainable Chem.*, 2021, **27**, 100393.
30 E. Catizzone, S. V. Daele, M. Bianco, A. Di Michele, A. Aloise, M. Migliori, V. Valtchev and G. Giordano, Catalytic application of ferrierite nanocrystals in vapour-phase dehydration of methanol to dimethyl ether, *Appl. Catal., B*, 2019, **243**, 273–282.
31 G. Yang, Y. Wei, S. Xu, J. Chen, J. Li, Z. Liu, J. Yu and R. Xu, Nanosize-enhanced lifetime of SAPO-34 catalysts in methanol-to-olefin reactions, *J. Phys. Chem. C*, 2013, **117**, 8214–8222.
32 H. Wu, M. Liu, W. Tan, K. Hou, A. Zhang, Y. Wang and X. Guo, Effect of ZSM-5 zeolite morphology on the catalytic performance of the alkylation of toluene with methanol, *J. Energy Chem.*, 2014, **23**, 491–497.
33 M. Albahar, C. Li, V. L. Zholobenko and A. A. Garforth, The effect of ZSM-5 zeolite crystal size on p-xylene selectivity in toluene disproportionation, *Microporous Mesoporous Mater.*, 2020, **302**, 110221.
34 X. Bai, J. Zhang, C. Liu, S. Xu, Y. Wei and Z. Liu, Solid-state NMR study on dealumination mechanism of H-**MOR** zeolite by high-temperature hydrothermal treatment, *Microporous Mesoporous Mater.*, 2023, **354**, 112555.
35 Y. Wang, J. Han, M. Chen, W. Lv, P. Meng, W. Gao, X. Meng, W. Fan, J. Xu, W. Yan and J. Yu, Low-silica Cu-**CHA** zeolite enriched with Al pairs transcribed from silicoaluminophosphate seed: synthesis and ammonia selective catalytic reduction performance, *Angew. Chem., Int. Ed.*, 2023, **62**, e202306174.
36 S. Liu, P. Zhang, X. Meng, D. Liang, N. Xiao and F.-S. Xiao, Cesium-free synthesis of aluminosilicate **RHO** zeolite in the presence of cationic polymer, *Microporous Mesoporous Mater.*, 2010, **132**, 352–356.
37 P. Feng, X. Bu and G. D. Stucky, Amine-templated syntheses and crystal structures of zeolite rho analogs, *Microporous Mesoporous Mater.*, 1998, **23**, 315–322.
38 S. Goel, S. I. Zones and E. Iglesia, Synthesis of zeolites via interzeolite transformations without organic structure-directing agents, *Chem. Mater.*, 2015, **27**, 2056–2066.
39 S. Inagaki, Y. Tsuboi, Y. Nishita, T. Syahylah, T. Wakihara and Y. Kubota, Rapid synthesis of an aluminum-rich **MSE**-type zeolite by the hydrothermal conversion of an **FAU**-type zeolite, *Chem. – Eur. J.*, 2013, **19**, 7780–7786.
40 S. Marković, V. Dondur, R. Dimitrijević and S. Macura, Thermallyinduced rings formation in aluminosilicate structures, *J. Therm. Anal. Calorim.*, 2006, **84**, 253–258.
41 M. Sakızcı and M. Özer, The characterization and methane adsorption of Ag-, Cu-, Fe-, and H-exchanged chabazite-rich tuff from Turkey, *Environ. Sci. Pollut. Res.*, 2019, **26**, 16616–16627.
42 Z. Zhang, Y. Li, Z. Chen, F. Ji, X. Liang, H. Xuan, L. Han and P. Han, TEAOH-assisted cost-effective preparation of SSZ-13 using L zeolite as Al source, *Fuel*, 2024, **362**, 130885.
43 H. Zhang, Q. Dong, P. Shan, D. Pan, B. Fan and R. Li, Synthesis of highly crystallized SSZ-13 with a small amount of organic structure-directing agent in the presence of seeds, *Microporous Mesoporous Mater.*, 2021, **324**, 111287.
44 J. G. Min, H. J. Choi, J. Shin and S. B. Hong, Crystallization mechanism of a family of embedded isoreticular zeolites, *J. Phys. Chem. C*, 2017, **121**, 16342–16350.
45 T. Inoue, M. Itakura, H. Jon, Y. Oumi, A. Takahashi, T. Fujitani and T. Sano, Synthesis of **LEV** zeolite by interzeolite conversion method and its catalytic performance in ethanol to olefins reaction, *Microporous Mesoporous Mater.*, 2009, **122**, 149–154.
46 J. C. Groen, R. Caicedo-Realpe, S. Abelló and J. Pérez-Ramírez, Mesoporous metallosilicate zeolites by desilication: On the generic pore-inducing role of framework trivalent heteroatoms, *Mater. Lett.*, 2009, **63**, 1037–1040.
47 J. Zhang, Y. Chu, X. Liu, H. Xu, X. Meng, Z. Feng and F.-S. Xiao, Interzeolite transformation from **FAU** to **CHA** and **MFI** zeolites monitored by UV Raman spectroscopy, *Chin. J. Catal.*, 2019, **40**, 1854–1859.
48 Z. Liu, A. Chokkalingam, S. Miyagi, M. Yoshioka, T. Ishikawa, H. Yamada, K. Ohara, N. Tsunoji, Y. Naraki, T. Sano, T. Okubo and T. Wakihara, Revealing scenarios of interzeolite conversion from **FAU** to **AEI** through the variation of starting materials, *Phys. Chem. Chem. Phys.*, 2022, **24**, 4136–4146.
49 M. J. Mendoza-Castro, E. De Oliveira-Jardim, N.-T. Ramírez-Marquez, C.-A. Trujillo, N. Linares and J. García-Martínez, Hierarchical catalysts prepared by interzeolite transformation, *J. Am. Chem. Soc.*, 2022, **144**, 5163–5171.
50 M. Chen, Y. Wei, J. Han, W. Yan and J. Yu, Enhancing catalytic performance of Cu-SSZ-13 for the $NH_3$-SCR reaction via in situ introduction of $Fe^{3+}$ with diatomite, *Mater. Chem. Front.*, 2021, **5**, 7787–7795.
51 M. Moliner, C. Franch, E. Palomares, M. Grill and A. Corma, Cu-SSZ-39, an active and hydrothermally stable catalyst for the selective catalytic reduction of $NO_x$, *Chem. Commun.*, 2012, **48**, 8264–8266.
52 N. Martín, C. R. Boruntea, M. Moliner and A. Corma, Efficient synthesis of the Cu-SSZ-39 catalyst for $DeNO_x$ applications, *Chem. Commun.*, 2015, **51**, 11030–11033.
53 J. Han, J. Li, W. Zhao, L. Li, M. Chen, X. Ge, S. Wang, Q. Liu, D. Mei and J. Yu, Cu-**OFF**/**ERI** zeolite: Intergrowth structure synergistically boosting selective catalytic reduction of $NO_x$ with $NH_3$, *J. Am. Chem. Soc.*, 2024, **146**, 7605–7615.
54 H. Sun, M. Wu, F. Han, W.-H. Wang, W. Wang, X. Luo and H. Chen, Crystallization of high silica **RHO** zeolite with self-assembled $Cs^+$-18-crown-6 sandwich complex, *Cryst. Growth Des.*, 2019, **19**, 3389–3396.

 

55 Y. Sasaki and M. Fukatsu, Selective catalysts for the production of nitrogen-containing compounds, *Catal. Surv. Asia*, 1998, **2**, 199–205.
56 H. Lee, J. Shin, W. Choi, H. J. Choi, T. Yang, X. Zou and S. B. Hong, PST-29: A missing member of the **RHO** family of embedded isoreticular zeolites, *Chem. Mater.*, 2018, **30**, 6619–6623.
57 U. Olsbye, S. Svelle, M. Bjørgen, P. Beato, T. V. W. Janssens, F. Joensen, S. Bordiga and K. P. Lillerud, Conversion of methanol to hydrocarbons: How zeolite cavity and pore size controls product selectivity, *Angew. Chem., Int. Ed.*, 2012, **51**, 5810–5831.
58 M. Guisnet, L. Costa and F. R. Ribeiro, Prevention of zeolite deactivation by coking, *J. Mol. Catal. A: Chem.*, 2009, **305**, 69–83.
59 M. S. Zanuttini, B. O. D. Costa, C. A. Querini and M. A. Peralta, Hydrodeoxygenation of m-cresol with Pt supported over mild acid materials, *Appl. Catal., A*, 2014, **482**, 352–361.
60 H. Geerts-Claes, G. Vanbutsele, S. P. Sree, S. Radhakrishnan, C. V. Chandran, E. Breynaert, J. A. Martens and S. Smet, **RHO** zeolites with high hydrothermal stability, *Cryst. Growth Des.*, 2023, **23**, 7829–7840.
61 C. Yao, J. Zhang and P. Liu, Application of domestic methylamine catalysts in large-scale facilities, *M-Sized Nitrogenous Fert. Prog.*, 2012, **5**, 18–20.
62 S. Yuvaraj, V. V. Balasubramanian and M. Palanichamy, N-Ethylation of aniline with ethanol or diethyl carbonate over alkali and alkaline zeolites Y and β, *Appl. Catal., A*, 1999, **176**, 111–117.
63 I. Mochida, A. Yasutake, H. Fujitsu and K. Takeshita, Selective synthesis of dimethylamine (DMA) from methanol and ammonia over zeolites, *J. Catal.*, 1983, **82**, 313–321.